Journal of Geophysical Research: Solid Earth

Supporting Information for

Upper mantle structure beneath the Mongolian region from multi-mode surface waves: Implications for the western margin of Amurian plate

Baigalimaa Ganbat[1,3], Kazunori Yoshizawa[1,2], Demberel Sodnomsambuu[3], Ulziibat Munkhuu[3]

[1]Department of Natural History Sciences, Graduate School of Science, Hokkaido University, Sapporo, Japan.

[2]Department of Earth and Planetary Sciences, Faculty of Science, Hokkaido University, Sapporo, Japan.

[3]Institute of Astronomy and Geophysics of Mongolia, Ulaanbaatar, Mongolia.

Contents of this file

Sections in this supplement

S1. Data set

Our dataset consists of around 87,000 paths for the fundamental-mode Rayleigh waves, about 50,000 paths for the fundamental-mode Love waves at 100 s, and about 20,000–50,000 paths for higher modes of both Rayleigh and Love waves (Figure S1). The period ranges for phase speed maps of each mode are summarized in Table S1.

Table S1. The period ranges of the multi-mode phase speed maps used to construct the 3-D S wave models of this study.

Mode	Rayleigh wave	Love wave
Fundamental mode	30.3 - 200.0 s	33.3 - 200.0 s
1st-higher mode	55.5 - 200.0 s	40.0 - 200.0 s
2nd-higher mode	55.5 – 200.0 s	62.5 - 166.7 s
3rd-higher mode	40.0 – 90.9 s	50.0 - 111.1 s
4th-higher mode	35.7 – 62.5 s	45.5 - 66.7 s

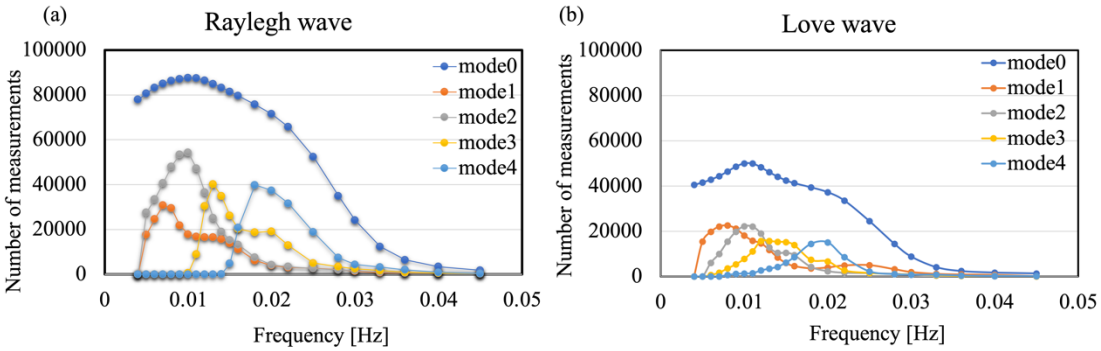

Figure S1. Numbers of measurements of multi-mode phase speeds for (a) Rayleigh waves and (b) Love waves as a function of period.

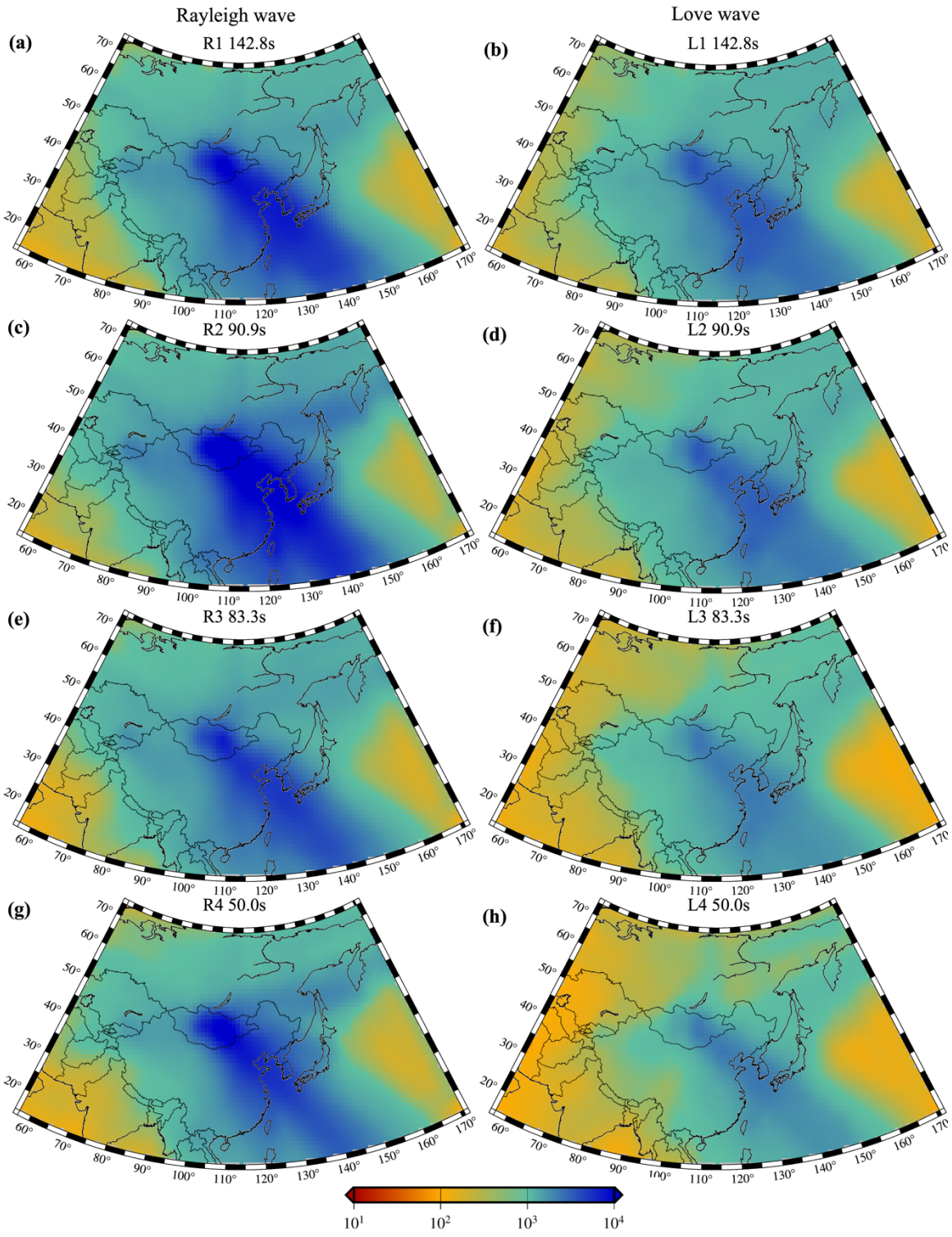

Figure S2. Ray-path density of the higher modes (1st - 4th) Rayleigh and Love waves. The number of rays counted in 2x2 (degree) grids.

S2. Resolution test

The spatial resolution of phase speed models is examined using checkerboard tests with various cell sizes, as displayed in Figure S3 for the fundamental and second higher-mode Rayleigh waves at 100 s, and in **Figure S4** for the fundamental and second higher-mode Love waves at 100 s.

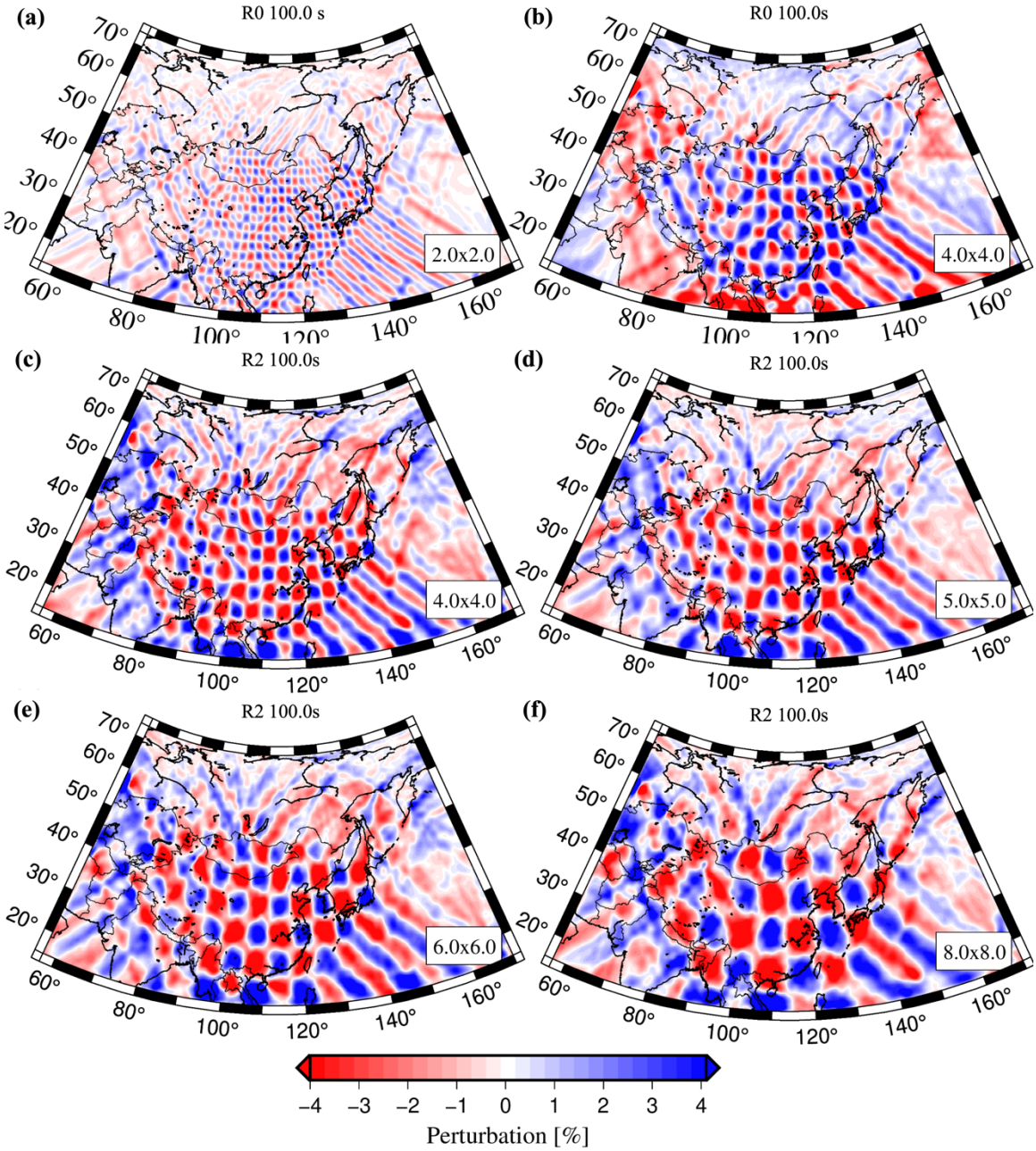

Figure S3. Results of checkerboard tests for the fundamental-mode Rayleigh waves at 100 s with (a) 3.0°, (b) 4.0°, and for the 2nd higher-mode Rayleigh waves at 100 s with (a) 4.0°, (b) 5.0°, (c) 6.0° and (d) 8.0° cells.

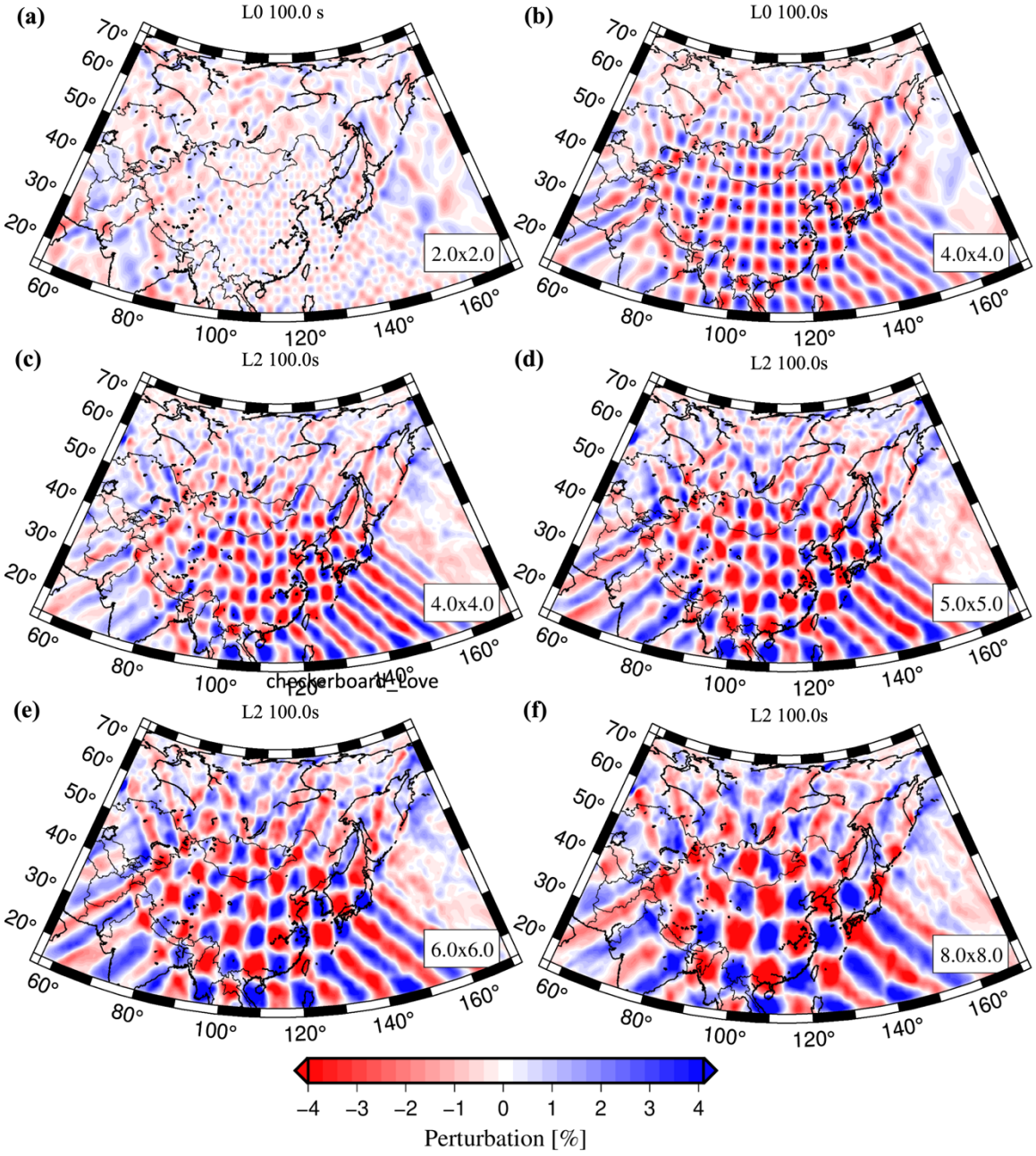

Figure S4. Results of checkerboard tests for the fundamental-mode Love waves at 100 s with (a) 2.0°, (b) 4.0°, and for the 2nd higher-mode Love waves at 100 s with (c) 4.0°, (d) 5.0°, (e) 6.0°, and (f) 8.0° cells.

S3. Jackknife resampling test

We performed jackknife resampling tests to estimate standard errors in our multimode phase speed maps. Jackknife resampling was made by randomly removing 10% of the original data, creating 10 sets (n = 10) of resampled data that were inverted independently for phase speed maps. The standard errors σ_{ij} of our phase velocity maps can be calculated as follows,

$$\sigma_{ij} = \sqrt{\frac{n-1}{n}\sum_{k=1}^{n}(v_{ij}(k) - \overline{v_{ij}})^2},$$

where *i* and *j* are the indices for latitude and longitude, respectively, *n* is the total number of resampled data sets, $v_{ij}(k)$ the phase speed of k-th resampled model, and $\overline{v_{ij}}$ the average phase speed of all resampled models. The results of the jackknife resampling test for the fundamental-mode Rayleigh wave at 100 s and the second higher-mode Love wave at 100 s are shown in Figure S5. The estimated errors for the fundamental-mode Rayleigh wave at 100 s are generally less than 0.052 km/s, and the errors tend to be larger in the northern part of Kazakhstan, while those for the second higher-mode Love wave at 100 s are around 0.11 km/s and the errors are larger in Tiksi, Yakutsk, and Kamchatka of Russia and the northern part of India.

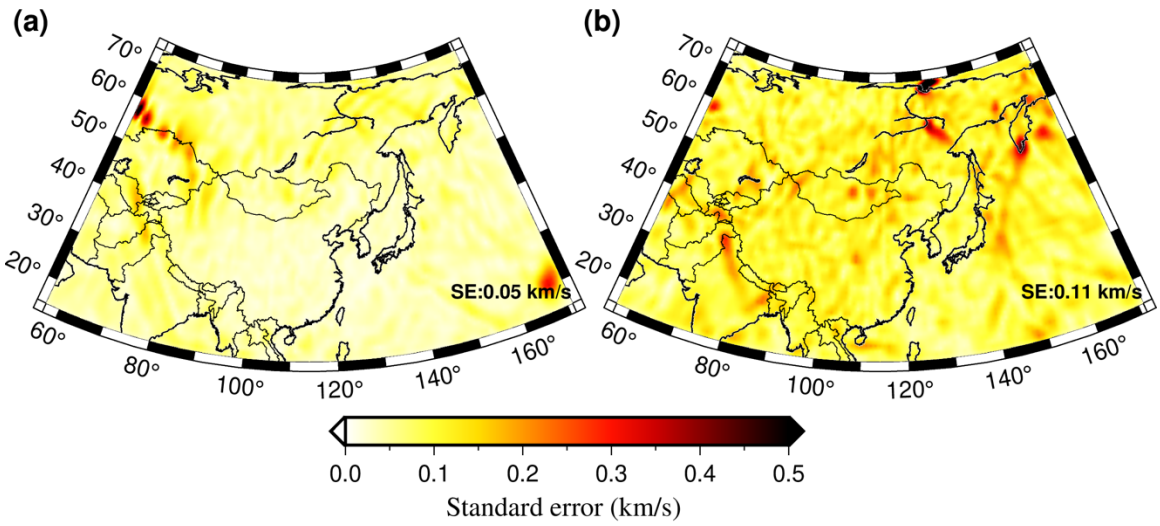

Figure S5. Results of jackknife resampling tests (a) for the fundamental-mode Rayleigh wave at 100 s, and (b) the second higher-mode Love wave at 100s

S4. Phase Velocity Map Gallery

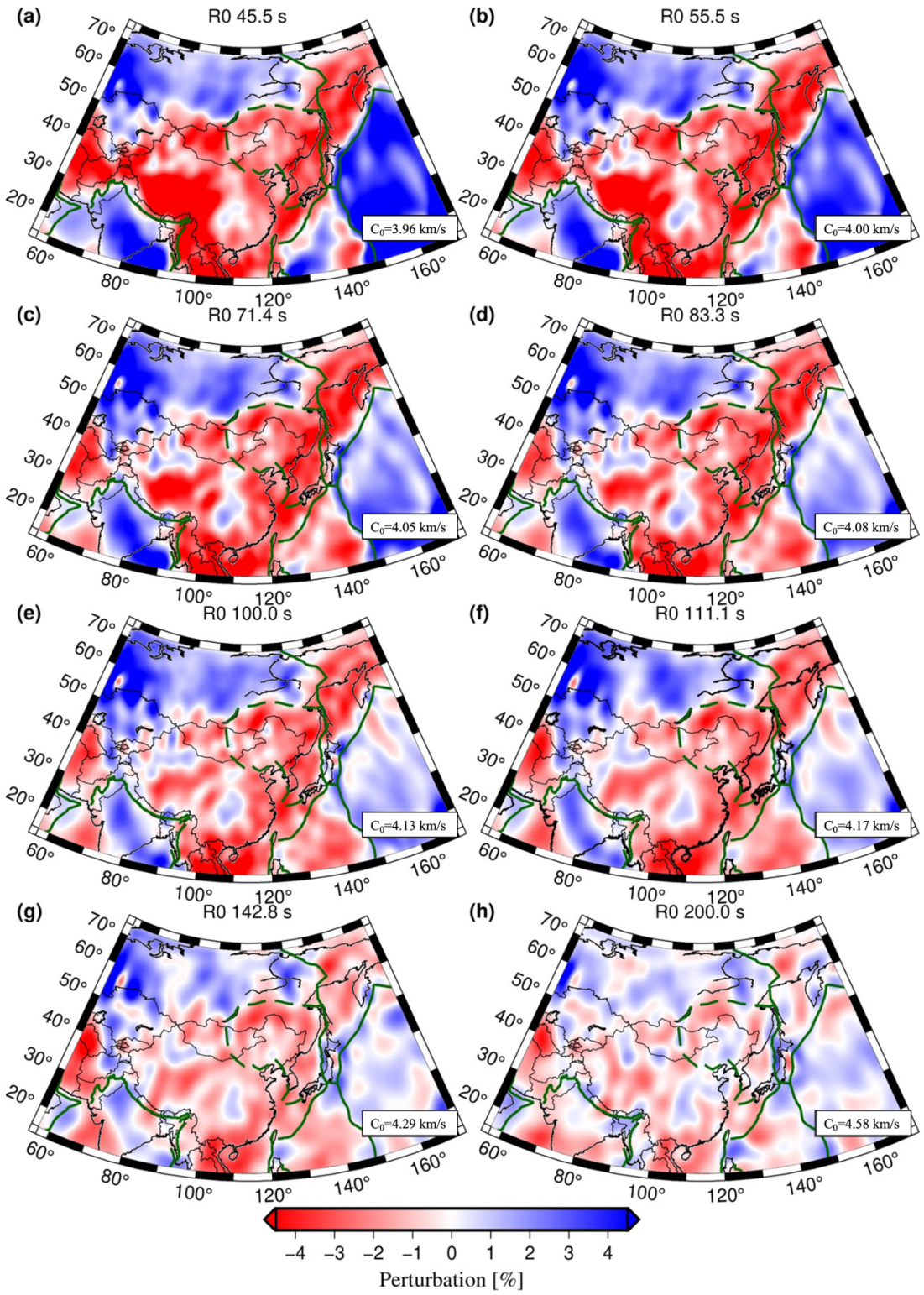

Figure S6. Phase speed maps for the fundamental-mode Rayleigh waves.

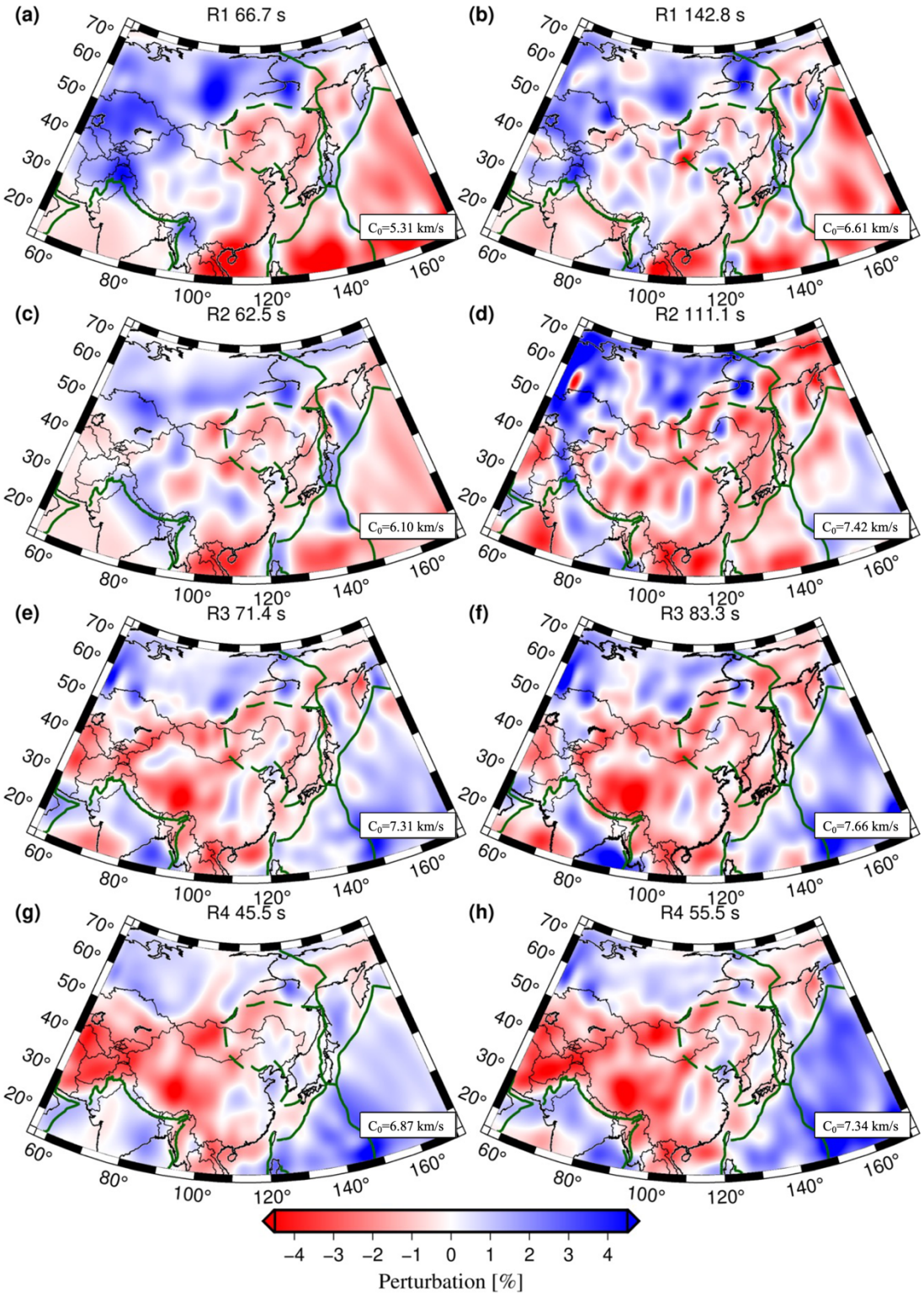

Figure S7. Phase speed maps for the higher-mode Rayleigh waves (1st - 4th higher modes).

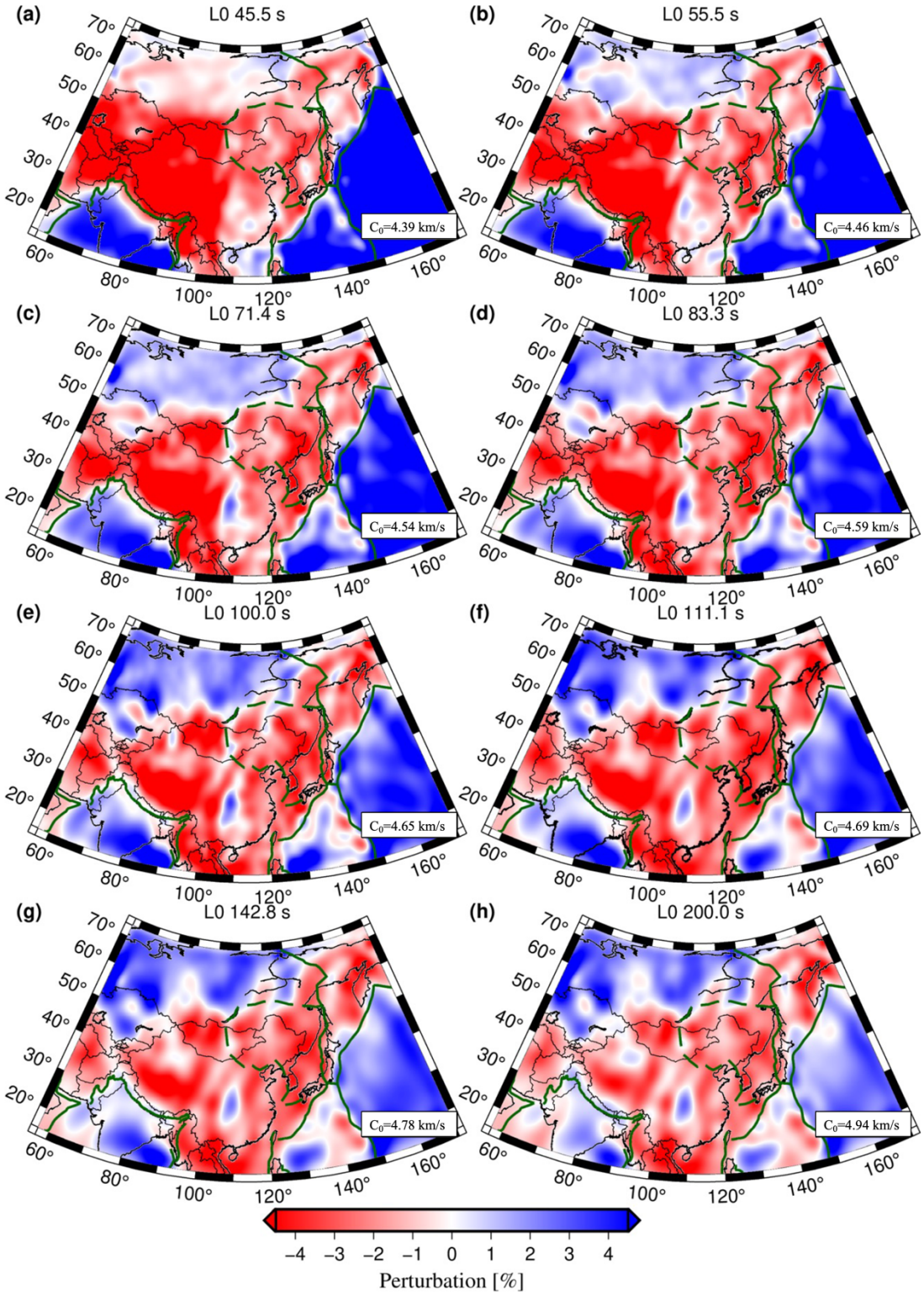

Figure S8. Phase speed maps for the fundamental-mode Love waves.

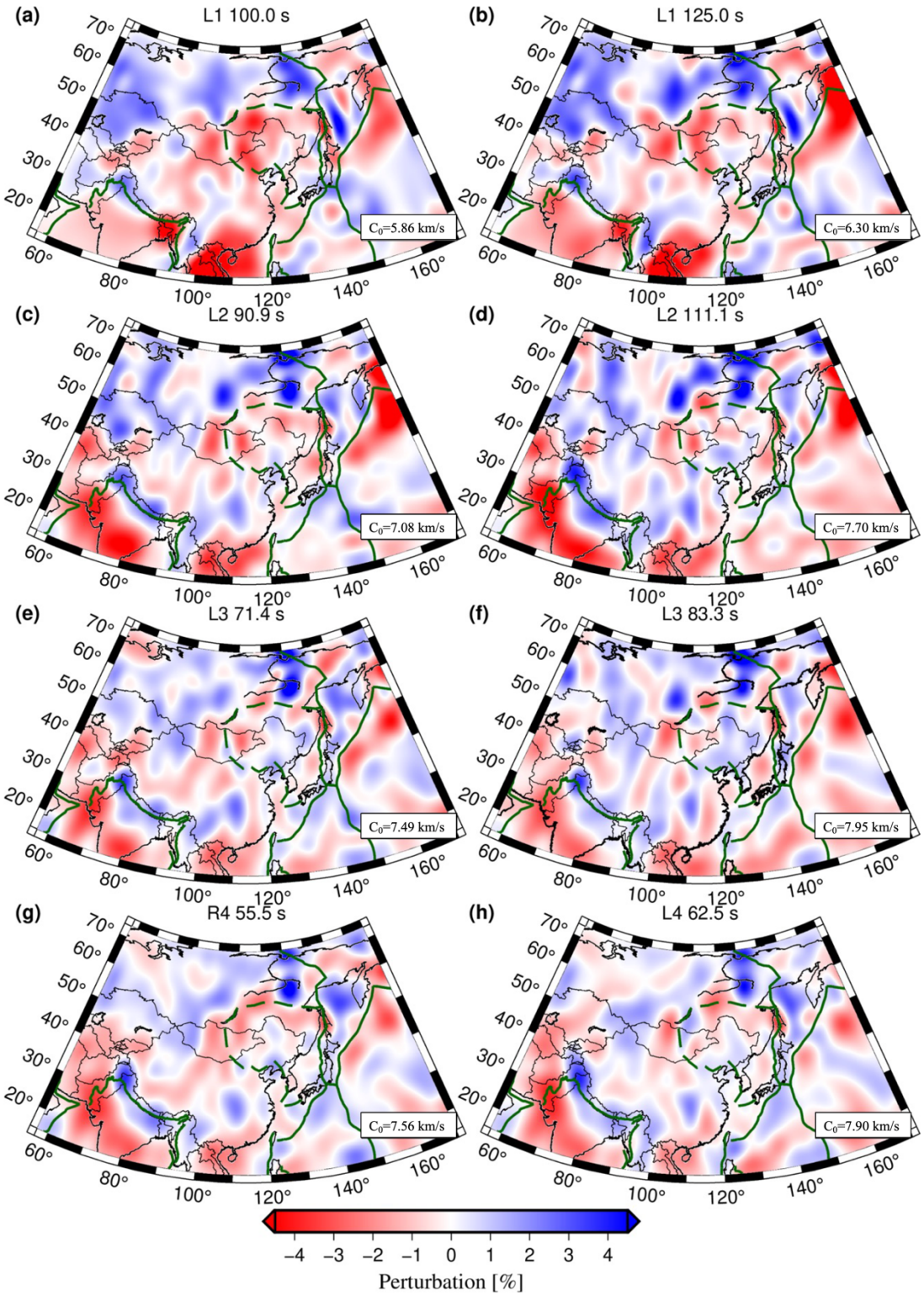

Figure S9. Phase speed maps for higher-mode Love waves (1st - 4th higher-modes).

S5. S-wave speed models

1-D S-wave profiles: The effects of crustal corrections

The influence of crustal corrections is investigated using two 3-D crust models, 3SMAC (Nataf & Ricard, 1996) and CRUST1.0 (Laske et al., 2013), and PREM (Dziewonski & Anderson, 1981) (i.e., without crustal correction). Below the Moho depth, we use a modified version of PREM (with smoothed 220 km discontinuity) as a reference mantle structure. Figure S10 compares the inverted SV models among different crustal corrections. Although there are some differences above 150 km depth, the crustal correction from the 1-D models has minor influence on the deep shear wave model below 150 km depth.

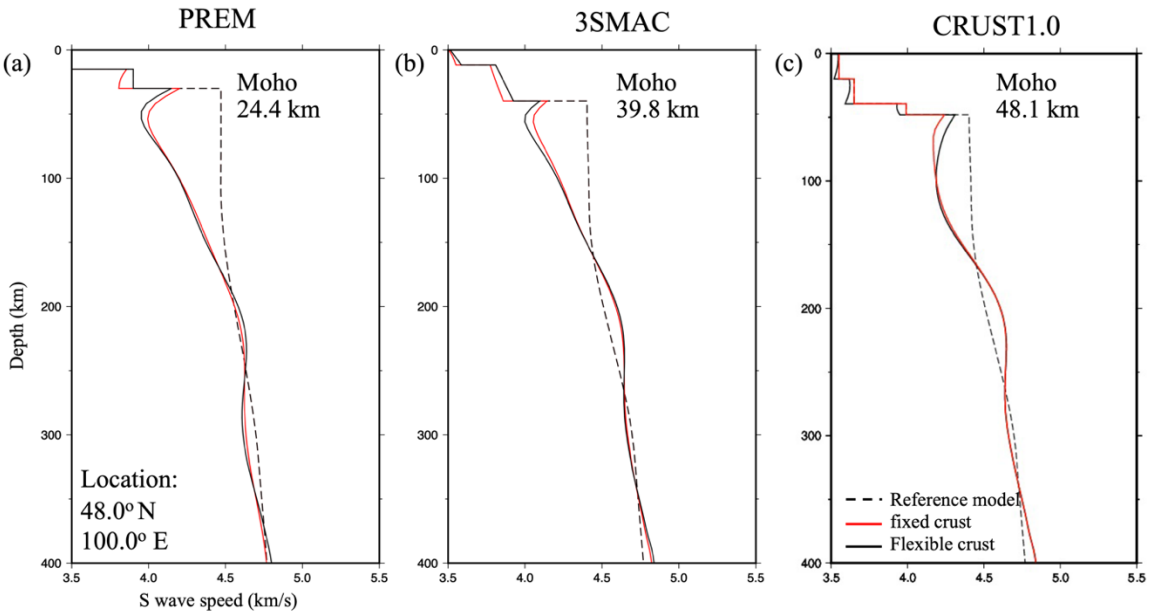

Figure S10. Example of S-wave models derived from the different crust models (PREM, 3SMAC, and CRUST1.0).

Vertical resolution tests

We performed the depth resolution tests (Figure S11). To generate synthetic dispersion curves for both Love and Rayleigh waves, including up to the fourth higher-modes, we create five synthetic models with a 5% faster anomaly in a limited depth range from 50 to 300 km. Then, using the same parameter sets for the real data inversions as explained in the main texts (section 4.1), radially anisotropic S-wave speed profiles are retrieved through the linearized inversions.

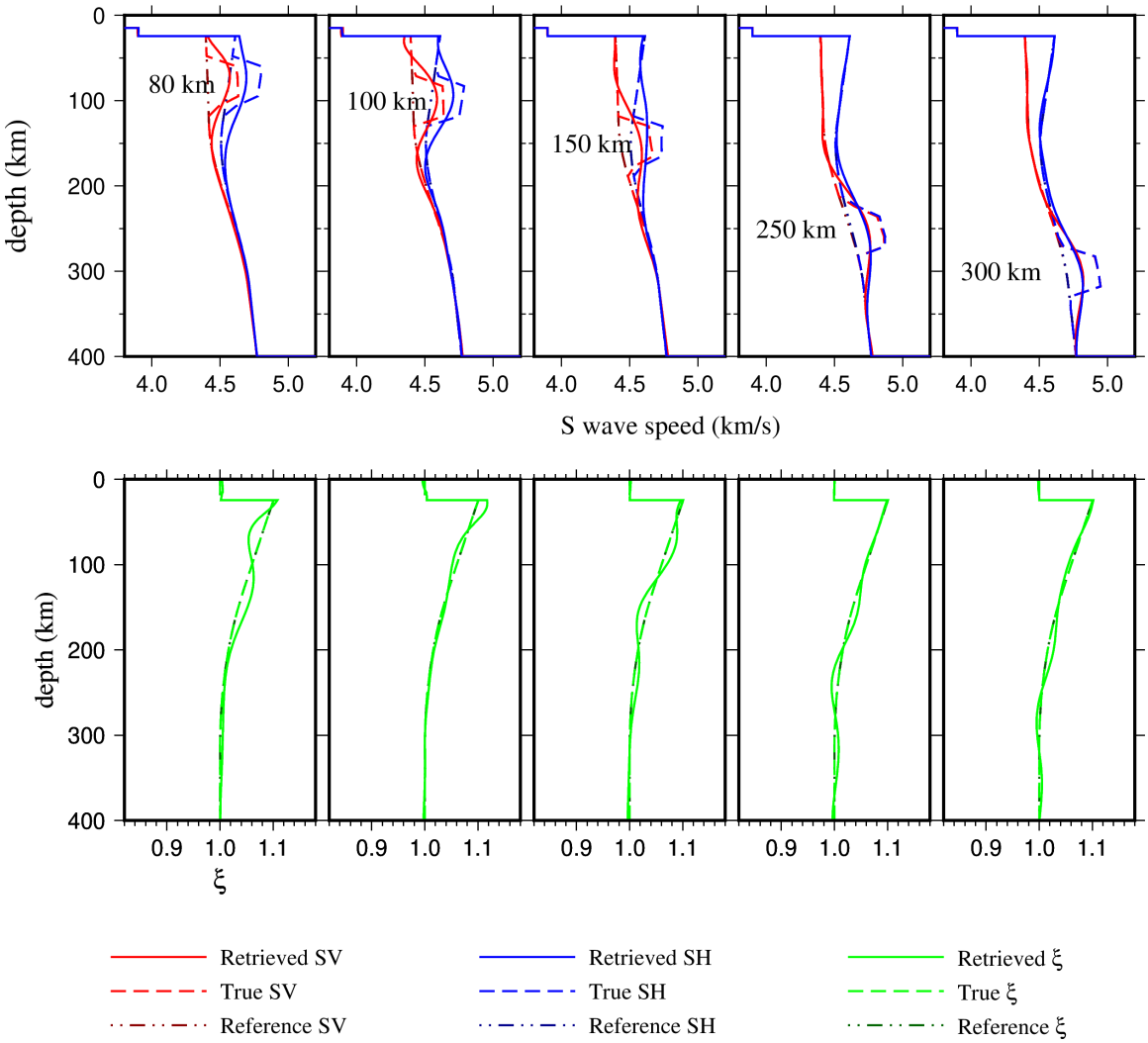

Figure S11. Examples of depth resolution tests for radially anisotropic shear wave models.

Average 1-D velocity profiles

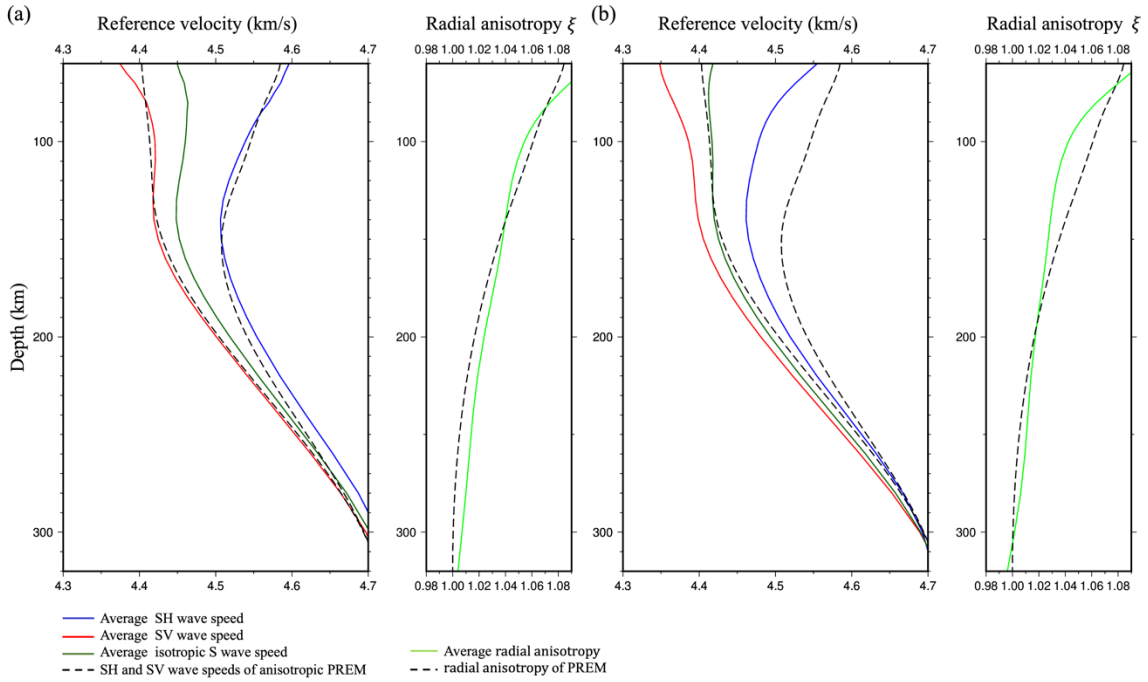

Figure S12. (a) The average velocity profiles of SV, SH, and isotropic S wave speeds in the whole region of this study, used as a reference model for the perturbation maps and cross sections in Figures 7 and S11-S16. (b) Same as (a) but in the Mongolian region, used as a reference model for the absolute S-velocity maps and cross sections in Figures 8 and S17-S20. Black dashed lines are SV and SH wave speeds of modified anisotropic PREM with the smoothed 220 km boundary.

3-D S-wave Model Gallery

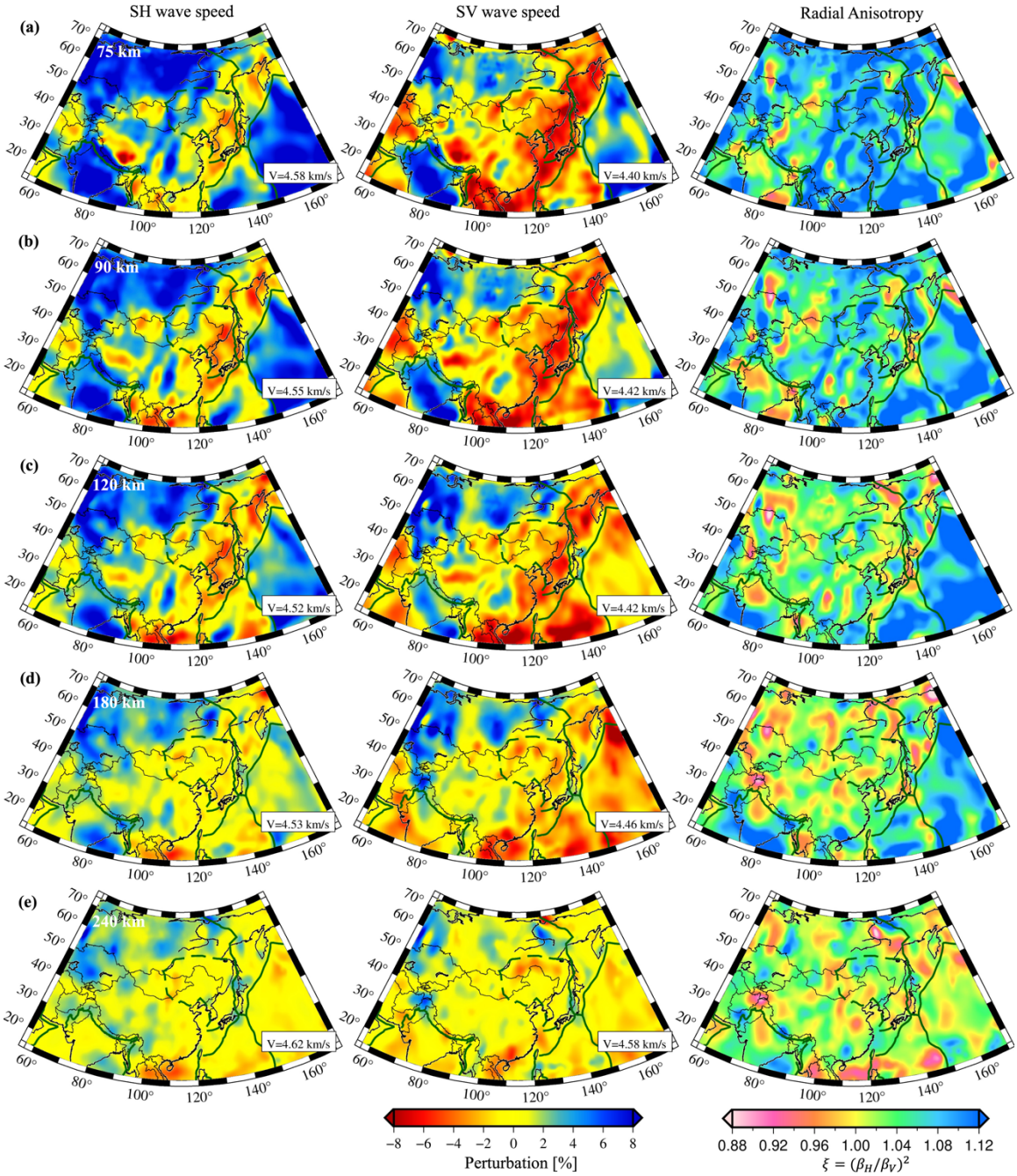

Figure S13. SH and SV wave speeds and radial anisotropy model of whole areas of this study.

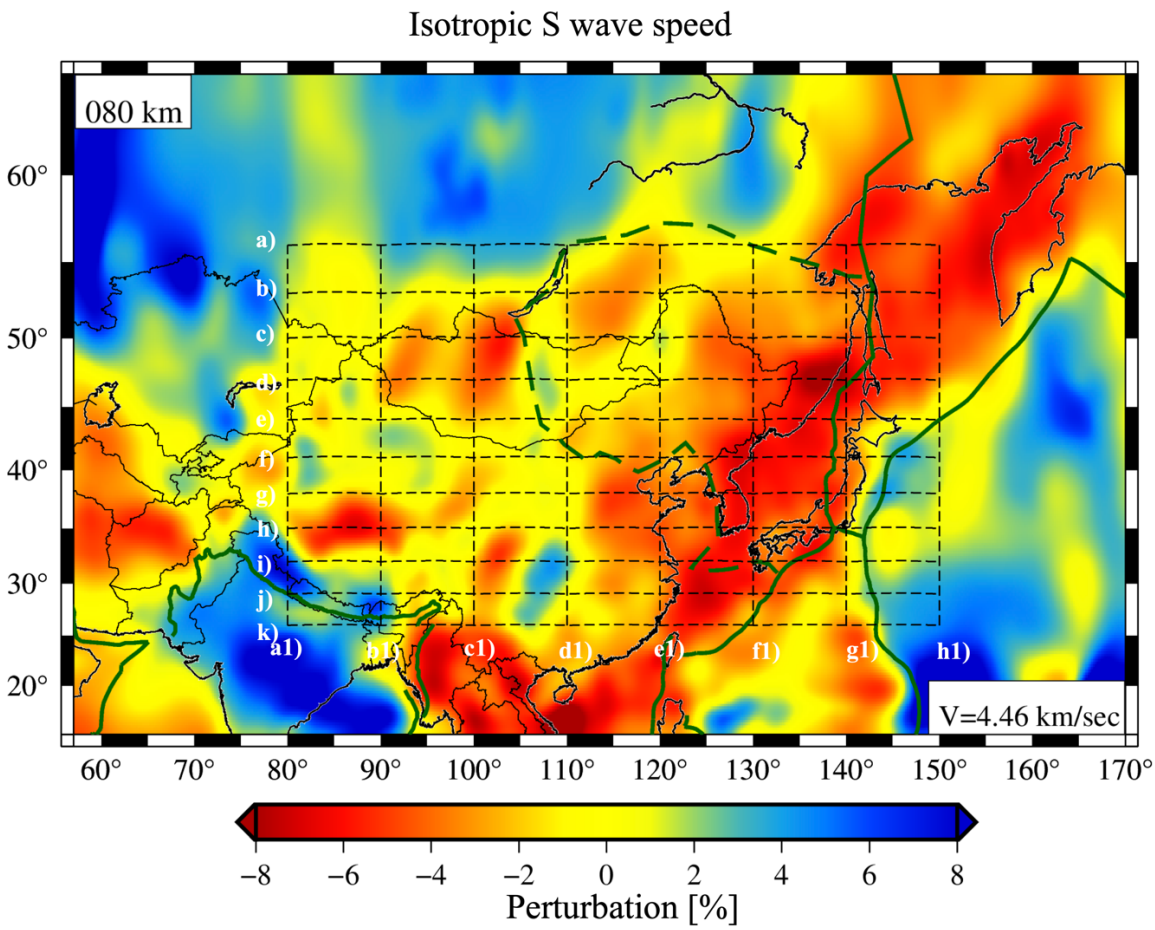

Figure S14. Isotropic S wave speed model at 80 km depth, indicating the locations of cross sections in Figs S15-S16.

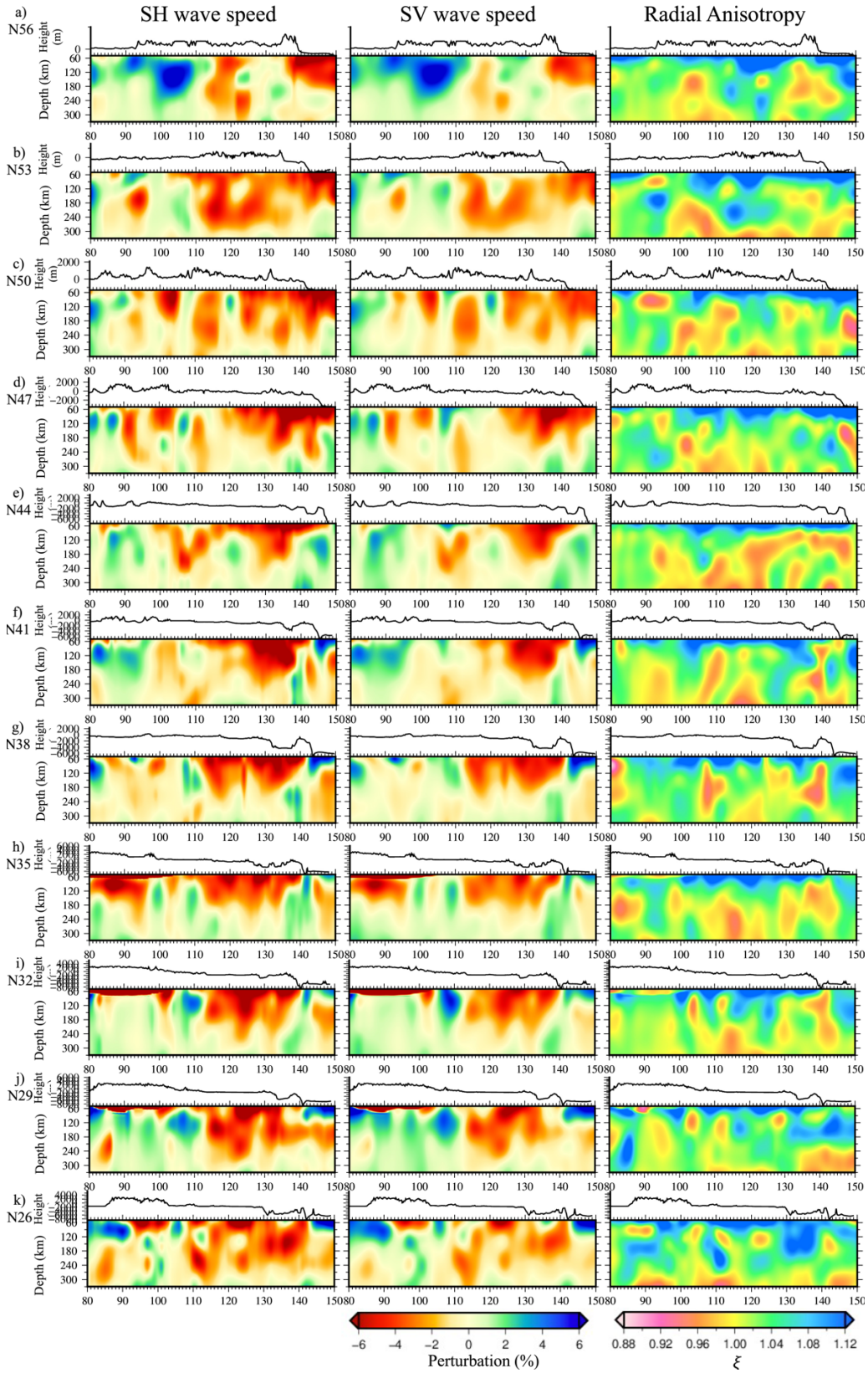

Figure S15. Vertical cross-sections of SH and SV wave speeds and radial anisotropy in W-E direction at latitudes from a) 56° to g) 26°.

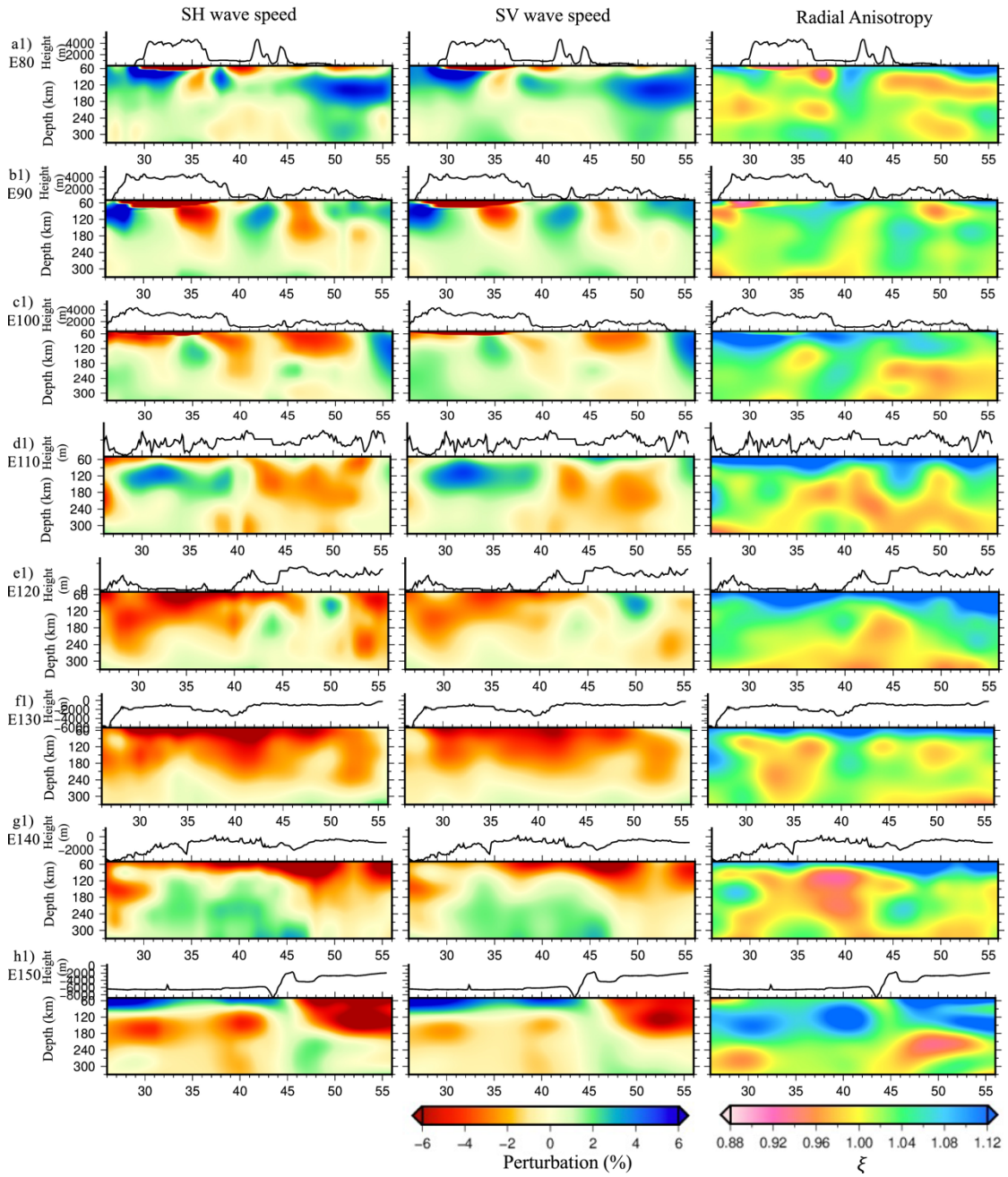

Figure S16. Vertical cross-section of SH and SV wave speed and radial anisotropy in S-N direction at longitudes from a) 80° to h) 150°.

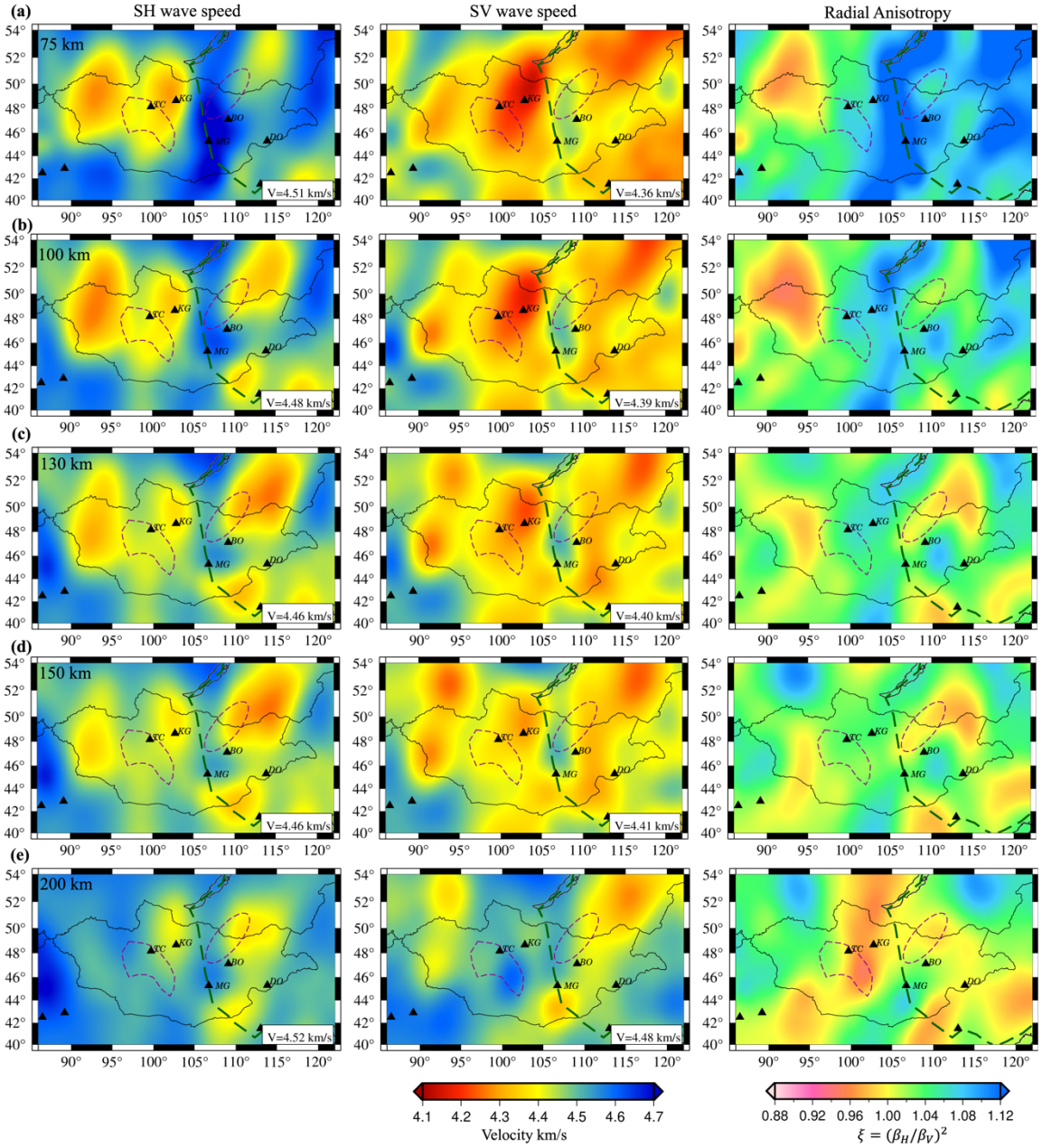

Figure S17. SH and SV wave speeds and radial anisotropy model beneath Mongolia.

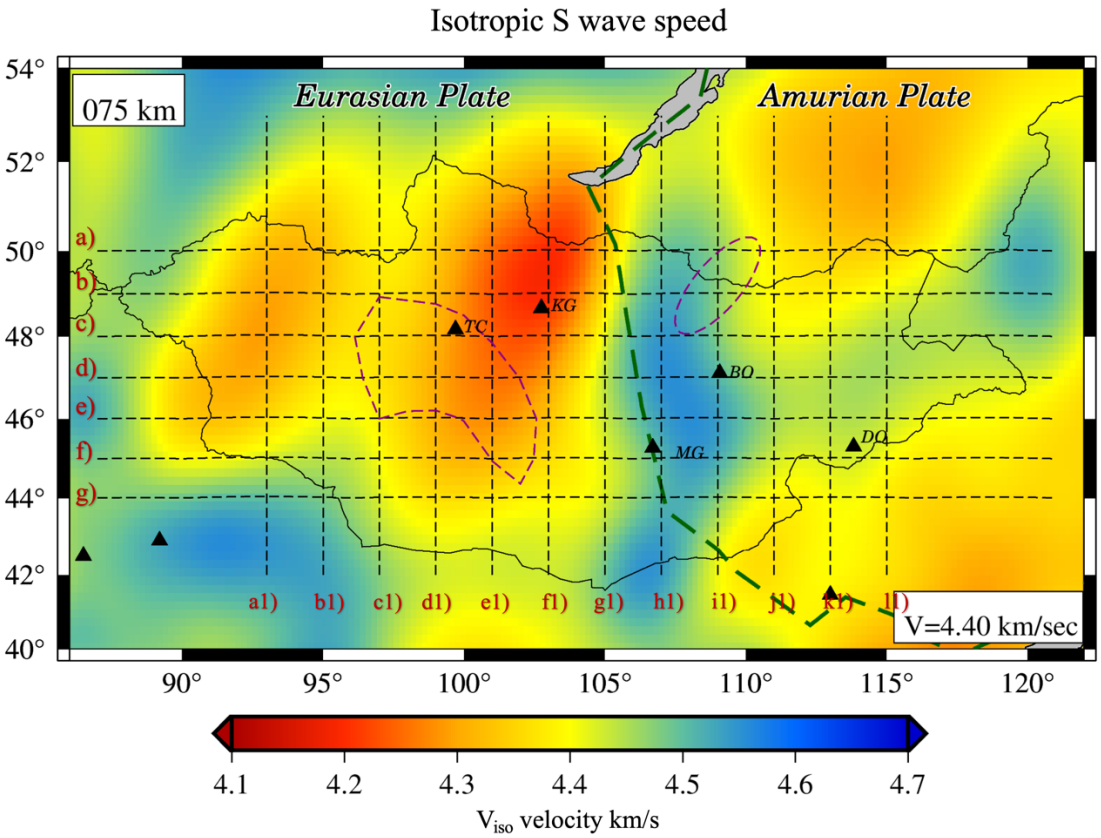

Figure S18. Isotropic S wave speed model at 75 km depth, indicating the locations of cross sections in Figs S19-S20.

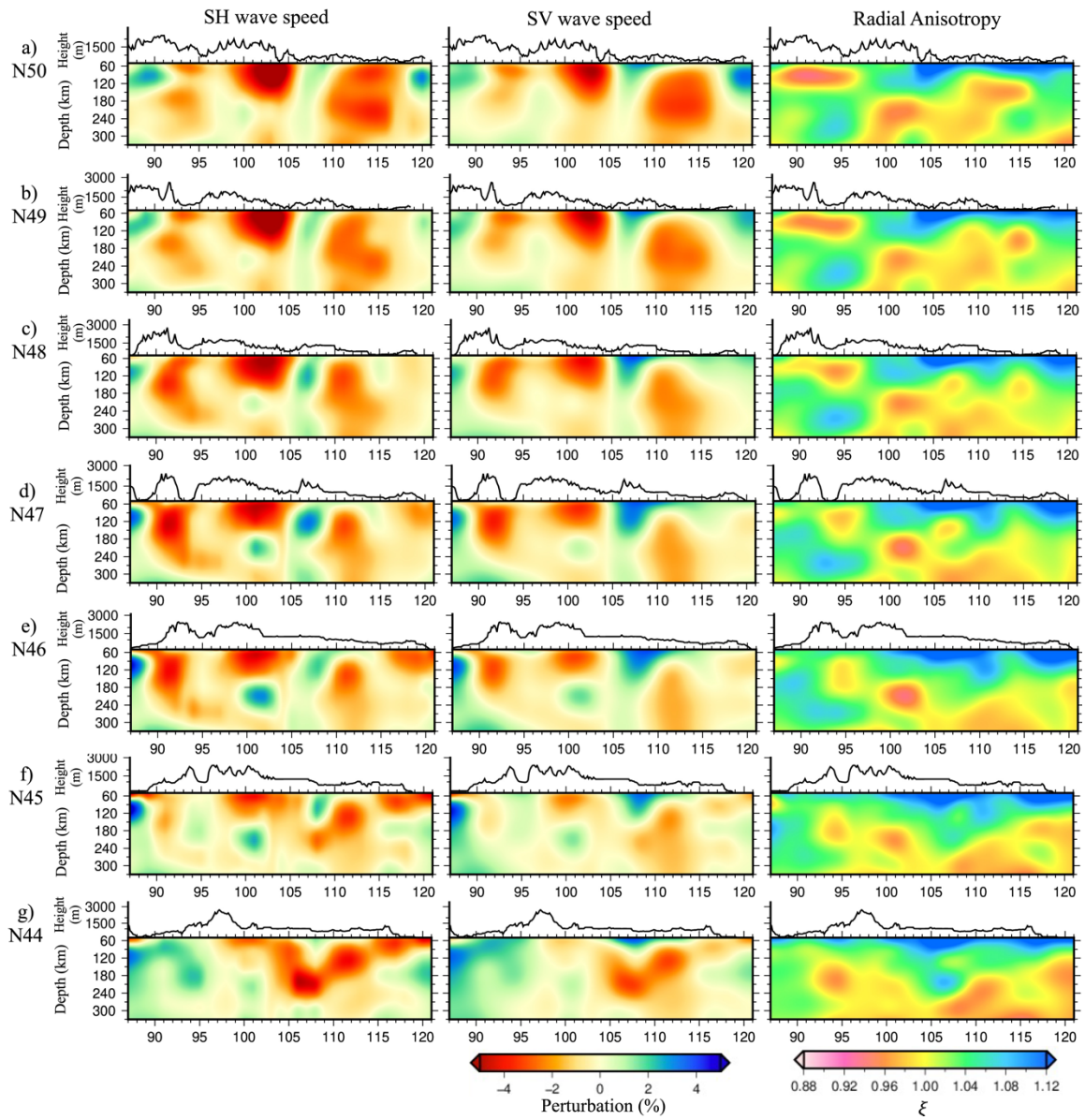

Figure S19. Vertical cross-sections of SH and SV wave speeds and radial anisotropy in W-E direction at latitudes from a) 50° to g) 44°.

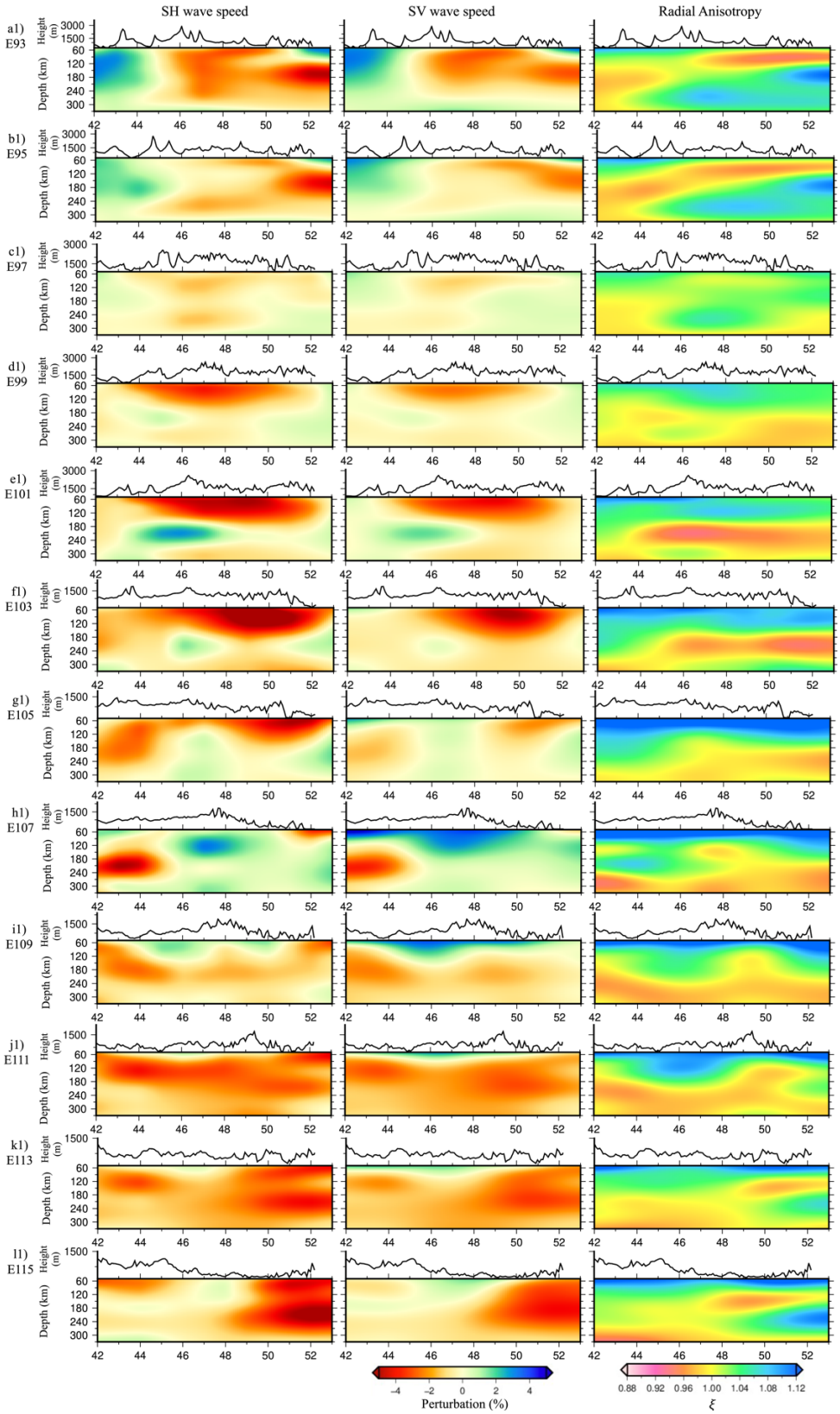

Figure S20. Vertical cross-sections of SH and SV wave speeds and radial anisotropy in S-N direction at longitudes from a1) 93° to l1) 115°.

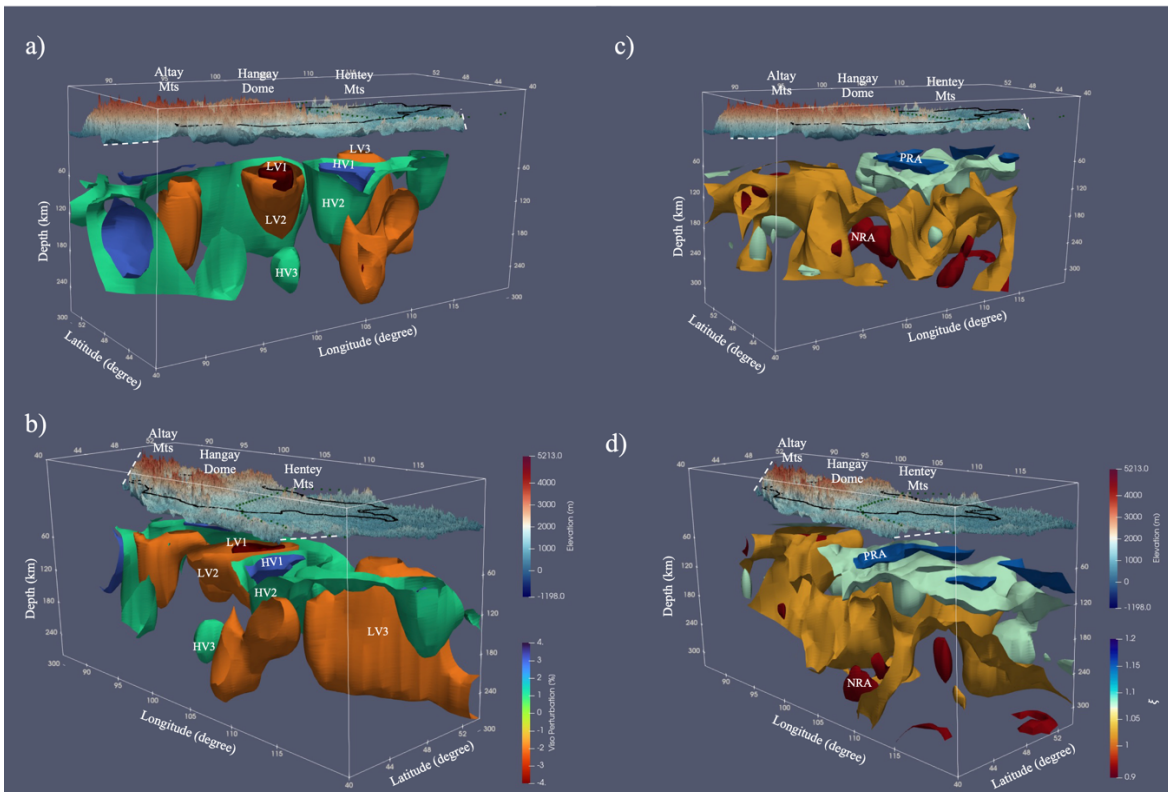

Figure S21. Three-dimensional visualization of (a, b) low and high shear wave speed anomalies and (c, d) radial anisotropy beneath the Mongolian region. Abbreviations of the labels: LV1 - lowest velocity beneath the Hangay Dome (-4 % isocontour); LV2 - low velocity beneath the Hangay Dome (-2% isocontour); LV3 - low velocity beneath the Hentey mountains (-2 % isocontour); HV1- highest velocity beneath the western margin of the Amurian plate (+3 % isocontour); HV2- high velocity beneath the western margin of the Amurian plate (+1.1 % isocontour); PRA-positive radial anisotropy (SH>SV) beneath the western margin of the Amurian plate (isocontour with $\xi = 1.15$); NRA-negative radial anisotropy (SV>SH) beneath the Hangay Dome (isocontour with $\xi = 0.96$).

References:

Dziewonski, A. M., & Anderson, D. L. (1981). Preliminary reference Earth model. Physics of the Earth and Planetary Interiors, 25(4), 297–356. https://doi.org/10.1016/0031-9201(81)90046-7

Laske, G., Masters, G., Ma, Z., & Pasyanos, M. (2013). Update on CRUST1.0---A 1-degree global model of Earth's crust. EGU General Assembly 2013, 15, 2658. Retrieved from http://meetingorganizer.copernicus.org/EGU2013/EGU2013-2658.pdf

Nataf, H. C., & Ricard, Y. (1996). 3SMAC: An a priori tomographic model of the upper mantle based on geophysical modeling. Physics of the Earth and Planetary Interiors, 95(1–2), 101–122. https://doi.org/10.1016/0031-9201(95)03105-7